PAPER

Check for updates

Spinel cobalt-based binary metal oxides as emerging materials for energy harvesting devices: synthesis, characterization and synchrotron radiation-enabled investigation†

Abdelelah Alshanableh,[a] Yusuf Selim Ocak,[ab] Bashar Aljawrneh, ID *[c] Borhan Aldeen Albiss,[a] Khaled Shawakfehc,[d] Latif U. Khane, ID [e] Messaoud Harfouchee[e] and Saja Alrousan[a]

The synthesis and characterization of spinel cobalt-based metal oxides (MCo_2O_4) with varying 3d-transition metal ions (Ni, Fe, Cu, and Zn) were explored using a hydrothermal process (140 °C for two hours) to be used as alternative counter electrodes for Pt-free dye-sensitized solar cells (DSSCs). Scanning electron microscopy (SEM) and atomic force microscopy (AFM) revealed distinct morphologies for each metal oxide, such as $NiCo_2O_4$ nanosheets, $Cu Co_2O_4$ nanoleaves, $Fe Co_2O_4$ diamond-like, and $Zn Co_2O_4$ hexagonal-like structures. The X-ray diffraction analysis confirmed the cubic spinel structure for the prepared MCo_2O_4 films. The functional groups of MCo_2O_4 materials were recognized in metal oxides throughout Fourier transform infrared (FTIR) analysis. The local structure analysis using X-ray absorption fine structure (XAFS) at Fe and Co K-edge identified octahedral (Oh) Co^{3+} and tetrahedral (Td) Co^{2+} coordination, with Zn^{2+} and Cu^{2+} favoring Td sites, while Ni^{3+} and Fe^{3+} preferred Oh active sites. Further investigations utilizing the Fourier transformation (FT) analysis showed comparable coordination numbers and interatomic distances ranked as Co–Cu > Co–Fe > Zn–Co > Co–Ni. Furthermore, the utilization of MCo_2O_4 thin films as counter electrodes in DSSC fabrication showed promising results. Notably, solar cells based on $CuCo_2O_4$ and $ZnCo_2O_4$ counter electrodes showed 1.9% and 1.13% power conversion efficiency, respectively. These findings indicate the potential of employing these binary metal oxides for efficient and cost-effective photovoltaic device production.

Introduction

Because of the permanent growth in the global population and industrialization, the demand for energy has increased steadily. Limits in fuel-based energy sources make the need for cleaner, sustainable alternative energy sources inevitable. Among all renewable energy sources, solar energy is one of the most impressive ones. Photovoltaic technologies, particularly dye-sensitized solar cells (DSSCs), have emerged as key factors in this transition owing to their low cost and easy production processes. Another important parameter that increases the impression of DSSCs is the capability of harvesting energy from even lower-intensive light.

Significant effort has been devoted to increasing the power conversion efficiency and stability of DSSCs while making them cost-effective. To achieve optimal performance in the DSSCs, the counter electrode commonly incorporates platinum (Pt) on a surface of transparent conductive oxide.[1,2] Several novel approaches have been formulated to improve the DSSCs' performance including enhancing the light absorption capacity of the sensitizer, charge separation of photo-induced charge at the electrolyte–semiconductor interface, and prompt the migration of charge towards the counter electrode.[3–5] The proposed approaches involve the binding of a sensitizer onto wide bandgap semiconductor substrates such as titanium dioxide, which aims to enhance light absorption capabilities.[6] Additional efforts have been made to replace the Pt counter electrode in DSSCs. As an alternative to Pt, various kinds of materials, including metal oxides, metal sulfides, carbon, and hybrid electrodes, have been proposed to obtain cost-effective

[a]Nanotechnology Institute, Jordan University of Science & Technology, PO Box 3030, Irbid 22110, Jordan

[b]Department of Physics and Engineering Physics, Morgan State University, Baltimore, Maryland 21234, USA

[c]Department of Physics, Al-Zaytoonah University of Jordan, PO Box 130, Amman 11733, Jordan. E-mail: B.Aljawarneh@zuj.edu.jo

[d]Department of Chemistry, Jordan University of Science & Technology, PO Box 3030, Irbid 22110, Jordan

[e]Synchrotron-Light for Experimental Science and Applications in the Middle East (SESAME), PO Box 7, Allan 19252, Jordan

device fabrication.[7–11] An alternative candidate with significant potential for DSSCs is spinel cobalt-based metal oxides (MB_2O_4, M: tetrahedral, B: octahedral sites). Such unique characteristics involve excellent electrical conductivity, efficient charge transfer, and significantly large surface area. Besides that, various oxidation states, and notable electrochemical activity make them highly advantageous to be used in energy and photocatalytic applications.[12–15]

The spinel cobalt oxide (Co_3O_4) is one of the most investigated electro-catalyst materials that is widely applied in the counter electrode for DSSCs. The tetrahedral site (Td) is occupied by Co^{2+} ions, while the octahedral site (Oh) is occupied by two Co^{3+} ions.[16] To date, Co^{2+} and Co^{3+} serve as active sites within the spinel cobalt metal oxide Co_3O_4, and they have been reported to have a crucial role in charge transfer and their catalytic activity.[17–19] Recent studies report that replacing the 3rd transition metal ions, such as Ni and Zn ions, with the Co^{2+} in spinel cobalt oxide (Co_3O_4) enhances their electrical conductivity.[20] For instance, $ZnCo_2O_4$ and $NiCo_2O_4$ exhibited superior electrical conductivity compared to Co_3O_4. Zn^{2+} ions are beneficial for indicating defects in the Td sites.,[17–20] as observed in spinel oxides, which in turn enhances the catalytic activity for the oxygen evolution reaction. Moreover, the large surface and electrical conductivity of $NiCo_2O_4$ result in better catalytic activity than spinel metal oxide (Co_3O_4). Also, the Fe^{3+} in $FeCo_2O_4$ occupies the Oh sites, leading to a shift in energy level near the Fermi level, which improves the activity of spinel metal oxide.[21,22]

Several reports have integrated the spinel-based cobalt structure into DSSC devices. Interestingly, the Co_3O_4 counter electrode of PCE ~8.6% in DSSCs exhibits an excellent catalytic performance towards the iodide electrolyte compared to the Pt standard counter electrode.[23] It has been reported also that, Co_3O_4 has a good electro-catalytic activity towards reduction of I_3^- ions into I^- ions.[24] Furthermore, zinc substitution for Co in cobalt oxide(II,III) results in the spinel structure of Zn–Co–O with p-type conductivity. The hole transport layer of Zn–Co–O

employed in DSSCs results in enhanced diffusion length and transport within a device.[25] The DSSCs based spinel $NiCo_2O_4$ nanostructures reported high performance and are comparable to the Pt counter electrode.[26] To address, the role of the local structure of the spinel-based cobalt materials in DSSCs performance still needs in-depth investigation.

In the present work, three-dimensionally arrays of spinel cobalt-based metal oxide thin films of MCo_2O_4 (M: Ni, Fe, Cu, Zn) were fabricated through hydrothermal deposition to use them as counter electrodes to obtain cost-effective DSSCs. Surface morphology and roughness of the prepared samples were investigated throughout SEM and AFM analysis. The XAFS technique is employed to examine the atomic coordination and interatomic distances by observing the local structure at Fe and Co K-edge. Also, the XANES spectra indicate the prepared samples have a spinel structure. Then, spinel cobalt-based metal oxide thin films were used in the fabrication of DSSCs as promising counter electrodes, and the photovoltaic performance of DSSCs with MCo_2O_4 counter electrodes were compared.

Experimental procedures

The following materials are used to synthesis the spinel cobalt based oxide films: copper nitrate tetrahydrate ($Cu(NO_3)_2 \cdot 4H_2O$), iron monohydrate ($Fe(NO_3)_2 \cdot H_2O$), nickel nitrate hexahydrate ($Ni(NO_3)_2 \cdot 6H_2O$), and zinc nitrate hexahydrate ($Zn(NO_3)_2 \cdot 6H_2O$), cobalt nitrate hexahydrate ($Co(NO_3)_2 \cdot 6H_2O$), hexamethylenetetramine (HMTA, $(CH_4)_6N_4$), and indium tin oxide (ITO) coated glasses, all are purchased from Sigma Aldrich and used without any further purification.

The samples were grown hydrothermally using a solution processing route. The synthesis of spinel cobalt-based metal oxide thin films, MCo_2O_4, coated over a cleaned ITO substrate is shown in Fig. 1. The ITO substrate was subjected to cleaning in the acetone for 15 min followed by 15 min in the ethanol under sonication. The preparation procedure was performed by
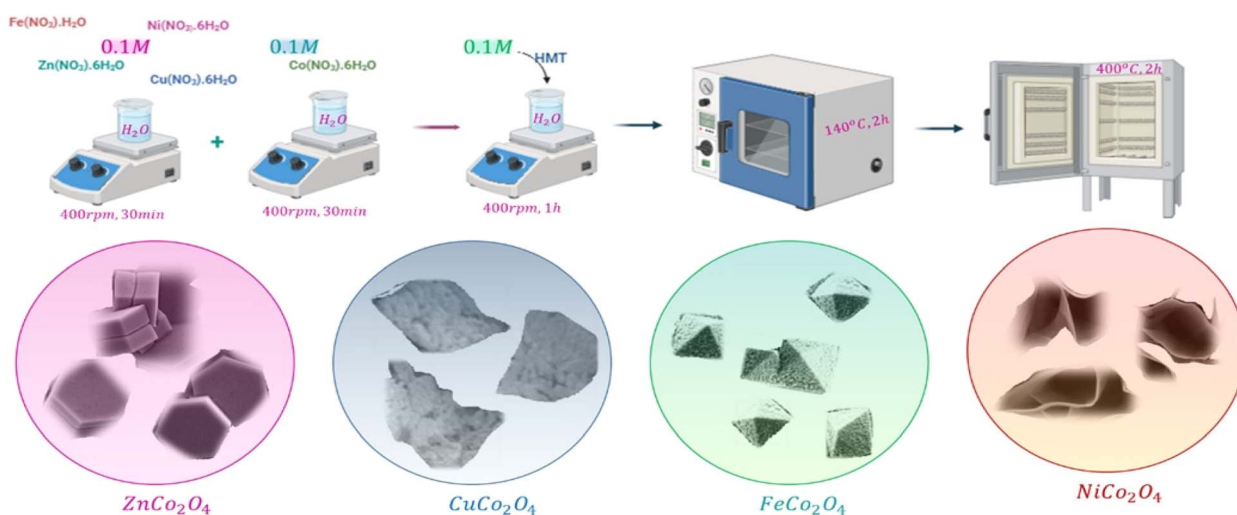

Fig. 1 A schematic illustration depicting the deposition procedures of spinel cobalt–based samples.

mixing 0.1 M of $M(NO_3)_2 \cdot xH_2O$ dissolved in 40 mL deionized water, and 0.1 M of $Co(NO_3)_2 \cdot 6H_2O$ dissolved in 40 mL deionized (DI) water. The solution was then stirred at 400 rpm for 30 min. Then, the 0.1 M of $(CH_2)_6N_4$ was added to the prepared aqueous solution. The obtained stock solutions were then transferred into a glass-sealed bottle containing a cleaned ITO substrate before being grown in an oven at 140 °C for two hours. Finally, the deposited spinel cobalt-based metal oxides of MCo_2O_4 films were rinsed with deionized water and annealed at 400 °C in a furnace for another two hours.

Scanning electron microscopy (SEM, Quanta FEG 450) was conducted to investigate the morphology and size distribution of the metal oxide samples. The surface roughness of the MCo_2O_4 thin films was carried out by using an atomic force microscope (AFM, SmartSPM™ 1000), FTIR (Bruker Vertex 80 and Hyperion 2000 microscope) used to investigate the vibrational modes and chemical bonds of metal oxides. The XAFS data were obtained *via* the BM-08 XAFS/XRF beamline at the Synchrotron-Light for Experimental Science and Applications in the Middle East (SESAME). The beamline was run in decay condition at an energy level of 2.5 GeV, with 300 mA as a maximum current. The X-ray absorption fine structure (XAFS) data were measured on the BM08-XAFS/XRF beamline of the SESAME operated at 2.5 GeV in "decay" mode with a maximum electron current of 300 mA.[27] The XAFS spectra of the materials were acquired in transmission mode in the spectral range of Co K-edge (7709 eV) and Fe K-edge (7112 eV) at room temperature. The X-ray beam intensity was measured by ionization chambers filled with an optimal mixture of noble gases at a total pressure of 1.0 bar, and the XAFS data of the samples were acquired from the signals measured at ion chambers subsequently amplified by Stanford picoammeters and digitalized by a voltage to frequency converter, using a double-crystal Si (111) monochromator. The energy was calibrated at the Co K-edge (7709 eV)

and Fe K-edge (7112 eV) of the Co and Fe standard metal foils, respectively. The sample was prepared in pallet form (13 mm diameter) by pressing a homogeneous mixture of calculated quantity of finely ground material and polyvinylpyrrolidone (PVP) powder. The amount of material in the pellet was calculated using XAFS mass software to give an absorption $\mu t \sim 1.5$, just above the Co K-edge and Fe–K edge absorptions.

The DSSCs were prepared using TiO_2 nanoparticle decorated ITO coated photoanodes. The electrodes were sintered at 450 °C in air ambient for 30 min to remove contaminations from the TiO_2 nanoparticle surfaces. And then was immersed in N719 dye for a night. The photoanodes were washed with ethanol and dried using a heat gun. MCo_2O_4 coated ITO counter electrodes and dye-coated TiO_2 photoanodes were sealed together and an electrolyte (iodide/tri-iodide in a nitrile solvent) was used to fill the space between two electrodes. The performances of DSSCs were measured under a class A solar simulator (ABET Technology Sun2000) with an AM 1.5 G filter and 100 mW cm^{-2} light intensity using a Keithley 2425 source meter.

Results and discussion

The DSSCs device performance is directly influenced by the morphology of the counter electrode in particular redox/oxidation electrolyte at the interface. SEM images can give insight into crystal arrays and defective surfaces of spinel cobalt oxides. The surface morphologies of as-prepared MCo_2O_4 thin films are illustrated in Fig. 2. Interestingly, the morphology of the prepared samples can be correlated to the variations in source metal ions. Fig. 2(a) and (b) manifested uniform arrays of nano-leave structures that coincide with the $CuCo_2O_4$ thin film. Whereas Fig. 2(c) and (d) displays uniform arrays of octahedral-shaped structures observed in the $FeCo_2O_4$ thin film. The $FeCo_2O_4$ thin film is comprised of nano-blocks with average size of about 500 nm. The observed octahedron structure
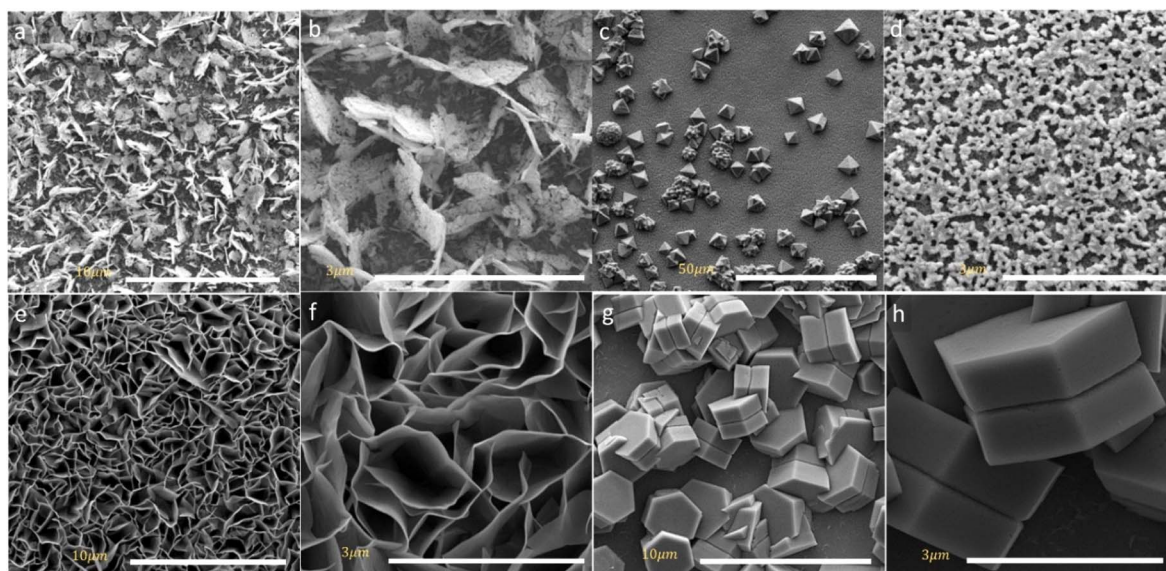

Fig. 2 SEM images of the obtained (a and b) $CuCo_2O_4$ thin film (c and d) $FeCo_2O_4$ thin film (e and f) $NiCo_2O_4$ thin film and (g and h) $ZnCo_2O_4$ thin film.

demonstrates high-pressure conditions controlled by the (111) plane, devoid of any preferential axis for selective growth.[28] Fig. 2(e) and (f) displays a hierarchical structure of $NiCo_2O_4$ nano-sheets observed with hollow arrays. Fig. 2(g) and (h) depicts a twin hexagonal configuration of nano-block $ZnCo_2O_4$ arrays observed with non-uniform distribution due to aniso-tropic growth along [100] and [001] directions.[29] It is impressive to find that different Zn^{2+}, Fe^{2+}, Ni^{2+}, and Cu^{2+} reacted species tend to form spinel structures in a cubic crystal phase. The intricate reaction pathways of these species during the hydro-thermal process drive the formation of distinct morphologies of spinel metal oxides. Initially, the decomposed reacted species undergo a recrystallization process to form MCo_2O_4 with pref-erential growth on selective planes, depending on the nature of the ions. The synthesis of MCo_2O_4 is driven by the formation of $M(OH)_2$ and $Co(OH)_2$ before transforming into $MCo_2(OH)_6$ complex compound, as demonstrated by the NR Chodankar group.[30] Alternatively, another reaction route suggests that the formation pathway is governed by the formation of Co_3O_4 and MO, which are then reduced to the MCo_2O_4 structure.[31] The annealing process reduces the OH^- ions in the complex compound to the oxide form, resulting in the obtaining of bimetal oxides.

The HMT acts as an alkaline source that assists in the formation of M–Co precursor. During the hydrolysis of HMT, NH_3 is released, making the solution alkaline. This process also produces OH^- ions in the hydrothermal synthesis, which react with Zn^{2+}, Fe^{2+}, Ni^{2+}, Cu^{2+}, and Co^{2+} ions to form spinel metal oxide. Furthermore, studies have found HMT useful for obtaining a crystalline spinel metal oxide structure. The alka-line environment facilitated by HMT is preferable for precipi-tating M^{2+} and Co^{2+} ions during hydrothermal deposition, accelerating the formation of the crystalline MCo_2O_4 structure.[32,33]

The surface area and roughness of the electrodes can provide significant insight into understanding the charge transfer

mechanism and overall device performance. The AFM imaging was performed for the MCo_2O_4 thin films and illustrated in Fig. 3. The AFM images of the prepared $CuCo_2O_4$ thin film exhibit a high root mean square (RMS) roughness of 0.16 μm and a large surface area of 38.74 μm². While the $FeCo_2O_4$ thin films show a polygon-shaped structure with an overall RMS of 0.03 μm and a surface area of 29.9 μm². The phase image demonstrates a variation between – 50° and 20° indicating low phase separation at the grain boundaries. The $NiCo_2O_4$ nano-sheets thin films depict a large surface area of 58.87 μm² and RMS of 0.26 μm with an average thickness of nearly 20 nm, while a high roughness was observed for the hexagonal struc-ture of $ZnCo_2O_4$ with an RMS of 0.35 μm and surface area of 34.9 μm². The hexagonal plates of $ZnCo_2O_4$ are stacked in a non-uniform structural array.

In DSSCs, the device performance is highly dependent on the crystal quality of the counter electrode based a binary metal oxide films. The cubic spinel structure was confirmed for various metal oxide films from crystallographic X-ray diffraction plots in Fig. S1.† As seen, the diffracted XRD peaks of $FeCo_2O_4$ film match the (220), (311), (400), (422), and (440) crystal planes indexed to $Fd3m$ space group (JCPDS card No. 04-0850). The crystal profile of $NiCo_2O_4$ nano-sheets assigned to (111), (220), (311), (222), (400), (331), and (511) crystal planes suggested $Fd3m$ space group (JCPDS card No. 01-073-1702). For $CuCo_2O_4$ nano-leaves, the observed XRD profile in agreement with (111), (220), (311), (400), (422), and (511) crystallographic planes analogue to $Fd3m$ space group (JCPDS card No. 23-1390). The $ZnCo_2O_4$ tends to form a crystal structure throughout hydro-thermal synthesis similar to the above metal oxide films. The crystal diffraction profile of $ZnCo_2O_4$ resembles (220), (311), (222), (511), and (620) crystal planes for $Fd3m$ (227) space group (JCDP card No. 00-001-1149).

The UV-vis-NIR spectral of the spinel metal oxide films plots in Fig. S2† and the corresponding extrapolated absorption band gap energies (E_g) were determined according to Tauc plot. The $NiCo_2O_4$ nanosheets exhibit higher absorbance compared to the other spinel materials oxides followed by crystal $CuCo_2O_4$ nanoleaves. The straight-line interception yields two band gap energies of 1.98 and 2.50 eV for $ZnCo_2O_4$, while the obtained band gap energies of 2.00 and 3.35 eV for $NiCo_2O_4$ in agreement with the reported values of 2.00 and 3.30 eV.[34] The valence band in $NiCo_2O_4$ was constructed from O 2p orbital and the conduction band from 3d orbitals of Ni and Co. And has an electron configuration of tetrahedral high spin Co^{2+} ($eg^4 t_2g^3$), octahedral low spin Co^{3+} (t_2g^6), and Ni^{3+} ($t_2g^6eg^1$). Therefore, the electron can be excited from Co-3d-t_{2g} to the partially filled Co 3d-eg orbital. Consequently, the presence of two band gap energies can be assigned to high spin and low spin of Co^{3+} in the spinel structure.[34] The spinel $CuCo_2O_4$ band gap energies was 1.88 eV and 3.0 eV and $FeCo_2O_4$ yields 2.18 eV and 2.82 eV. The determined values are close to those reported in the literature.[35,36]

The solution processed DSSCs device *via* hydrothermal usually contains –OH functional group. To verify the presence of the –OH group and other functional groups that could influence the device performance, the FTIR profile illustrated in Fig. 4
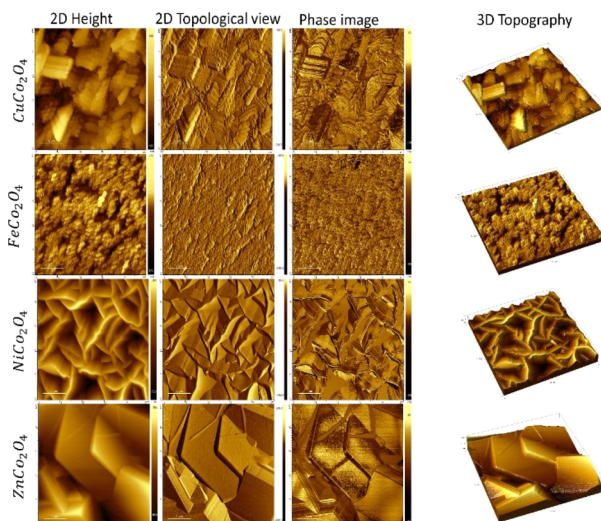

Fig. 3 AFM images of as-deposited metal oxides of $NiCo_2O_4$, $CuCo_2O_4$, $ZnCo_2O_4$, $NiCo_2O_4$, and $FeCo_2O_4$ in 2D and 3D profile.
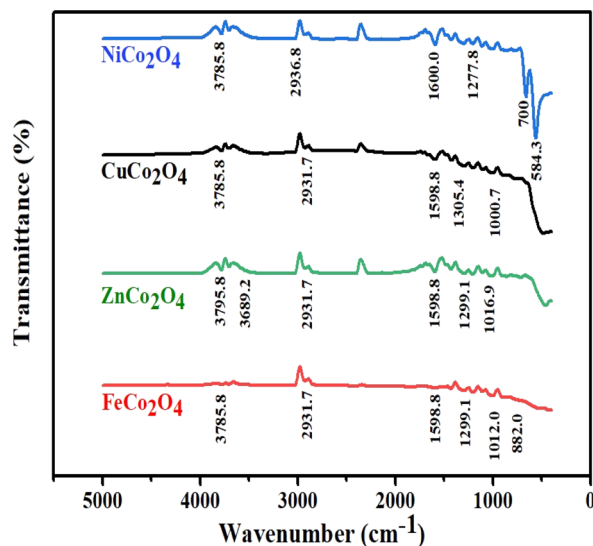
Fig. 4 FTIR profile of the prepared binary metal oxide films MCo_2O_4.

Fig. 5 XANES spectra collected at Fe and Co K-edge of (a) $NiCo_2O_4$, (b) $ZnCo_2O_4$, and (c) $CuCo_2O_4$ collected at Co K-edge and (d) $FeCo_2O_4$ collected at Fe kedge; inset figures illustrate the corresponding first derivative of the absorption spectra.

corresponds to the prepared MCo_2O_4 films. The vibration modes that match the M–O group can be seen at 584.3 cm^{-1} in various sample profiles. The M–O vibration modes at 584.3 cm^{-1} and 700 cm^{-1} may be associated with octahedral and tetrahedral sites.[37] Furthermore, stretching modes located at approximately 882 cm^{-1} and 1000 cm^{-1} are assigned to the C–O group. Furthermore, the weak vibrational mode at 1277.8 cm^{-1} and 1299.1 cm^{-1} is linked to the NO_3^- group.[38] Additional stretching characteristics identified at 1598.8 cm^{-1} and 1600 cm^{-1} were assigned to COO and C=O molecules.[39] The stretching modes at 2931.7 cm^{-1}, 2936.8 cm^{-1}, 3785.8 cm^{-1}, and 3795.8 cm^{-1} are attributed to the O–H functional group.[40,41] A higher content of OH– molecules was noticed in the case of $ZnCo_2O_4$ associated with a prominent shift in the OH vibration mode.

The local structure of the MCo_2O_4 thin films could play an effective role in the DSSC device performance. The applied XAFS integrates to resolve the local structure of spinel cobalt oxide devices. The XANES spectra at Co absorption K-edge are presented in Fig. 5 of the prepared samples. Resolving the $FeCo_2O_4$ structure at the Co absorption K-edge is elusive and therefore XANES is applied at the Fe absorption K-edge. According to the XANES data, the Co absorption K-edge was (7722.53 eV) for $NiCo_2O_4$, (7724.02 eV) for $CuCo_2O_4$ and (7722.18 eV) for $ZnCo_2O_4$. The observed Co absorption K-edge aligns with the value reported in the literature at 7721.4 eV, while the Fe absorption K-edge was 7125.53 eV for $FeCo_2O_4$. The oxidation state of the cobalt cation is Co^{3+} and the observed XANES spectrum reveals the spinel structure of the prepared samples.[42,43]

The observed XANES spectrum reveals a low-intensity pre-edge peak at A, which can be assigned to 1s → 3d quadrupole transition in spinel cobalt oxide (Co_3O_4).[44] A transition edge (shoulder region) was observed at B, along with the prominent white-line peak of high intensity at C. These transition edges at
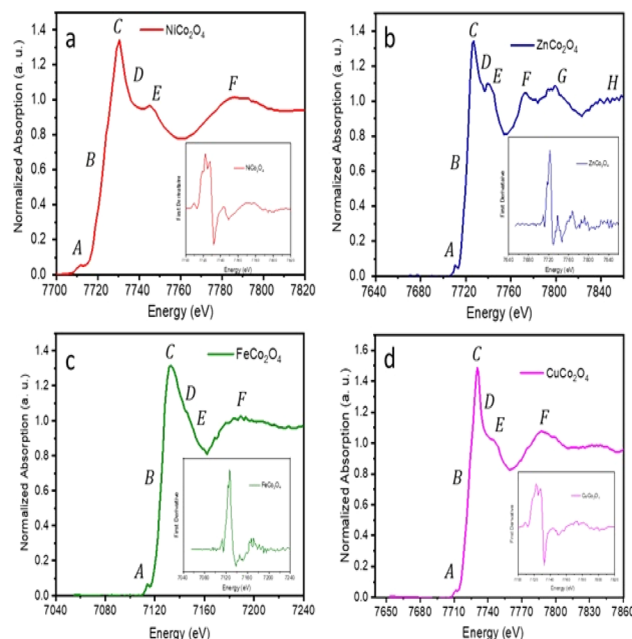
B and C can be attributed to resonance peaks.[45,46] The white-line region can be ascribed to the 1s → np transition.[46]

Following that, minor peaks of low intensity were observed at D and E. The broadening of peak D, in particular, in $FeCo_2O_4$ can be attributed to the coordination atoms in the vicinity of the Co absorber atom. Moreover, two peaks at E and F indicate the presence of multiple scattering associated with the coordination of the medium-range structure surrounding the Co absorber atom.[47,48] Furthermore, two peaks at G and H were observed in the XANES spectrum coinciding with the $ZnCo_2O_4$ sample, which can be attributed to the existence of multiscattering effects.

To facilitate a comprehensive quantitative analysis of the local atomic structure of the MCo_2O_4 nanomaterials, the EXAFS fitting in R-space was conducted.[49] The experimental EXAFS data in R-space in the range of 1.0 to 5.0 (Å) with Hanning window and k range of 3.0 Å^{-1} were analyzed to the best fit. The initial four high-ranking single scattering paths of Co–O and M–Co bond pairs were included in the fit. The passive electrons reduction factor S_0^2 and energy shift E_0 were set similarly for all the paths in the fit, and the mean-square relative displacement σ^2 and interatomic distance R were refined relatively to get the best fit result.

Fig. 6 plots k^3-weighted EXAFS with the best fit, and the FT, respectively. The fit parameters with details are listed in Table 1. The FT analysis of spinel $FeCo_2O_4$ structure shows a strong peak around 1.500 Å assigned to the Fe–O_1 (2.239 Å) coincides with T_d Fe^{2+} and Fe–O_2 (1.963 Å) assigned to O_h Fe^{3+}. The Fe–Co_1 and Fe–Fe_1 bonds are observed near the 3 Å which reveals the Co^{2+} cations are substituted by Fe^{2+} cations in the spinel Co_3O_4 structure ($FeCo_2O_4$). The Fe–Co^1 can be resolved to O_h Fe^{3+} and
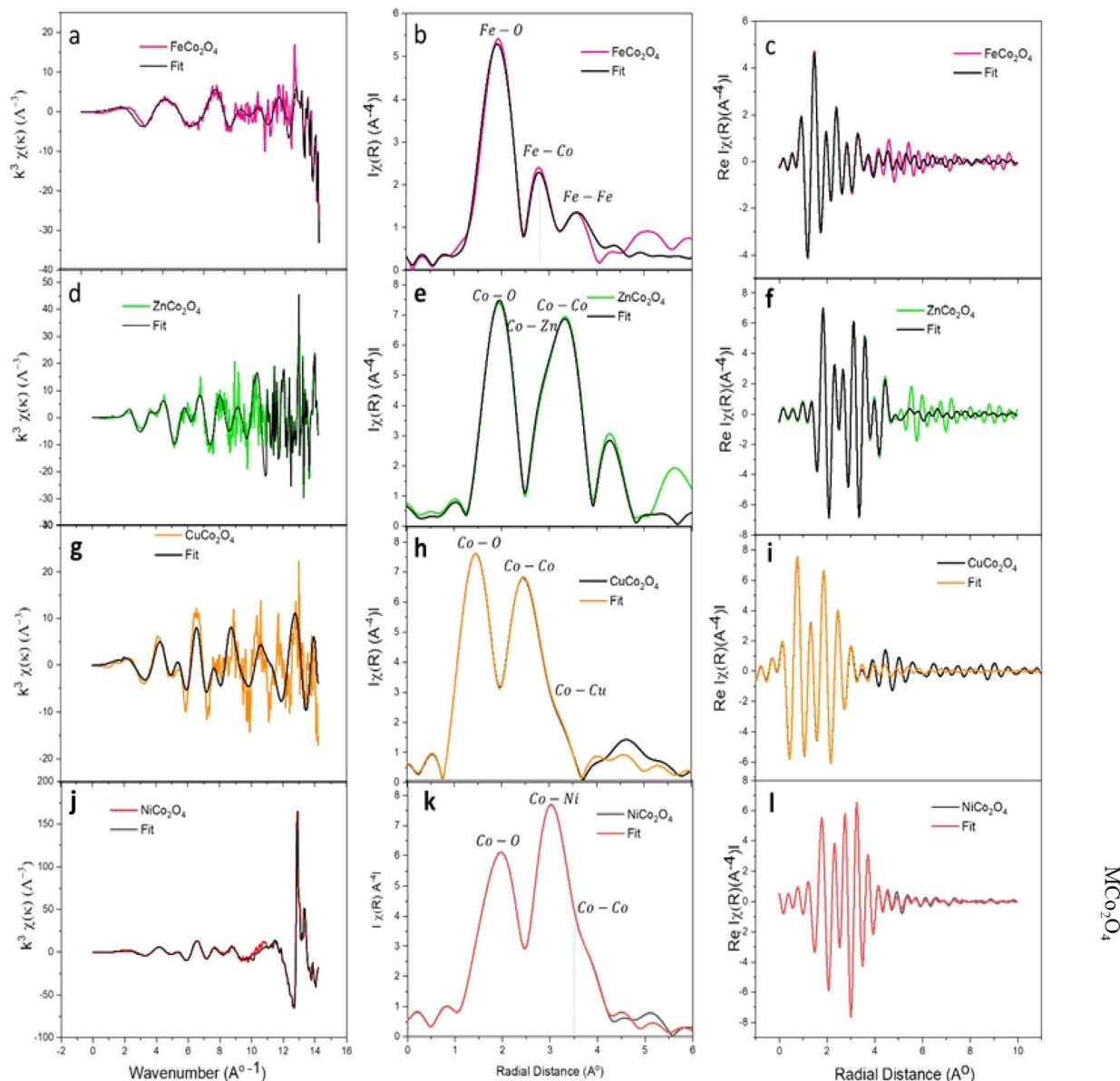
Fig. 6 k^3-weighted EXAFS data with the best fit from Co and Fe K-edge absorption, FT, and the Re (FT) of the EXAFS data, respectively for (a−c) FeCo$_2$O$_4$, (d−f) ZnCo$_2$O$_4$, (g−i) Cu Co$_2$O$_4$ and (j−l) NiCo$_2$O$_4$ samples.

T_d Co^{2+} sites. According to the reported data, the Fe, Cu, and Ni cations exhibit a tendency to occupy the octahedral sites (O$_h$) and leave tetrahedral (T$_d$) sites in spinel Co$_3$O$_4$.[50] On the other side, the Co^{2+} ions in the Co$_3$O$_4$ compound are substituted by Zn^{2+} ions, which exhibit tetrahedral symmetry (T$_d$), leading to the formation of ZnCo$_2$O$_4$.[46] Interestingly, the ZnCo$_2$O$_4$ tends to form a spinel structure as the Zn^{2+} occupy the tetrahedral sites (T$_d$) and leaving the Co^{3+} at octahedral sites (O$_h$).[51] The crystal ZnCo$_2$O$_4$ has a spinel structure (A^{2+}Co$_2$$^{3+}O_4$, where, A is tetrahedral and B is octahedral sites) closely similar to the Co$_3$O$_4$ structure.[51] Indeed, the FT shows Co–O$_1$ (1.966 Å) interaction, which is characteristic of O$_h$ Co^{3+}. Also, the Co–Zn$_1$ bond suggested T$_d$ Zn^{2+} and O$_h$ Co^{3+} in the spinel structure of ZnCo$_2$O$_4$. The Co–O$_1$ and Co–Co$_1$ own octahedral symmetry. This finding shows a good agreement with the previous reports that

confirmed the CoO$_6$ structure has octahedral symmetry, whereas the CoO$_4$ exhibits tetrahedral symmetry.[52] Furthermore, the results imply that the Zn^{2+} cations have a tendency to occupy active sites characterized by a low oxidation state, whereas Co^{3+} cations are left in octahedral locations. It is clear that T$_d$ Zn^{2+} and O$_h$ Co^{3+} ions were presented in the crystalline structure of the ZnCo$_2$O$_4$ spinel structure.

Moreover, the FT first peak at 1.900 Å interatomic distance in spinel CuCo$_2$O$_4$ structure corresponds to the Co–O$_1$ (1.917 Å) of Oh Co^{3+} and Co–O$_2$ (2.058 Å) of T$_d$ Co^{2+}. The results in accordance with the previous reports.[51,53] The FT peak at 3.200 Å is correlated to Co–Co$_1$ (3.237 Å) and Co–Cu1 (3.462 Å) bond interactions. It has been reported that the Co–Co interactions can be found in Oh and Td as Co^{3+}–Co^{3+} (2.85 Å), Co^{3+}–Co^{2+} (3.346 Å), and Co^{2+}–Co^{2+} (3.495 Å).[54] Therefore, the Co–Co1

Table 1 EXAFS fitting parameters, including coordination number (N), mean coordination shell radii (R), mean square relative displacements (MSRDs) or Debye–Waller factor (σ^2), amplitude reduction factor (S_o^2), photoelectron energy (E_o) and goodness of the fit (R_{factor}) for the MCo_2O_4 binary metal oxides

Sample	Bond type	N	R (Å)	σ^2 (Å²)	S_o^2	E_o (eV)	R_{factor}
$CuCo_2O_4$	Co–O$_1$	2	1.917 ± 0.010	0.0023 ± 0.0044	1	0.530	0.1057
	Co–O$_2$	2	2.058 ± 0.091	0.0147 ± 0.0423	1	0.530	0.1057
	Co–Co$_1$	2	3.237 ± 0.150	0.0094 ± 0.0057	1	0.530	0.1057
	Co–Cu$_1$	4	3.462 ± 0.067	0.0066 ± 0.0087	1	0.530	0.1057
$NiCo_2O_4$	Co–O$_1$	2	1.912 ± 0.017	0.0009 ± 0.0020	1	0.679	0.0103
	Co–O$_2$	4	1.940 ± 0.174	0.0238 ± 0.0072	1	0.679	0.0103
	Co–Ni$_1$	4	2.835 ± 0.042	0.0037 ± 0.0088	1	0.679	0.0103
	Co–Co$_1$	2	2.988 ± 0.078	-0.0015 ± 0.0099	1	0.679	0.0103
$ZnCo_2O_4$	Co–O$_1$	4	1.966 ± 0.036	0.0045 ± 0.0023	1	0.250	0.0571
	Co–O$_2$	6	3.808 ± 0.166	0.0045 ± 0.0268	1	0.250	0.0571
	Co–Zn$_1$	4	3.197 ± 0.058	0.0057 ± 0.0038	1	0.250	0.0571
	Co–Co$_1$	6	3.439 ± 0.234	0.0001 ± 0.0303	1	0.250	0.0571
$FeCo_2O_4$	Fe–O$_1$	2	2.239 ± 0.173	0.0056 ± 0.027	1	0.527	0.0320
	Fe–O$_2$	4	1.963 ± 0.105	0.0045 ± 0.0054	1	0.527	0.0320
	Fe–Co$_1$	4	3.224 ± 0.252	0.0006 ± 0.0123	1	0.527	0.0320
	Fe–Fe$_1$	2	3.409 ± 0.266	-0.0015 ± 0.012	1	0.527	0.0320

interactions in spinel $CuCo_2O_4$ assigned to O_h Co^{3+} and T_d Co^{2+}. Moreover, the Co–Cu$_1$ bridges the T_d Cu^{2+} and T_d Co^{2+}.

The above-reported XANES (Fig. 5b) pre-edge of $NiCo_2O_4$ suggested the presence of T_d Co^{2+} symmetry.[55] It can be preliminary concluded that, the $NiCo_2O_4$ is close to the spinel Co_3O_4 structure and the oxidation state for both is 8/3 as oxidation state corresponding to the presence of O_h Ni^{3+}.[56] The FT analysis of $NiCo_2O_4$ reveals a peak at the lowest interatomic distance of 1.94 Å assigned to Co–O$_1$ of O_h $(Co^{3+}O_6)$ and Co–O$_2$ of T_d $(Co^{2+}O_4)$.[57] The next FT peak at 2.9 Å corresponds to Co–Co$_1$ (2.988 Å) and 4Co–Ni$_1$ (2.835 Å) interactions. It's evident the Co–Co$_1$ is characteristic of Oh Co^{3+} and the Co–Ni1 coincides characteristic of O_h Co^{3+} and the Co–Ni$_1$ coincides with O_h Co^{3+} and O_h Ni^{3+}. In general, the Co–O interatomic distances at T_d or O_h sites are shorter than M–O distances which is correlated with a small atomic radius of Co^{3+} in comparison with M^{2+}. It is obvious that the Co–O$_1$ and Co–O$_2$ in $ZnCo_2O_4$ are longer compared to other spinel structures. It is worth noting that, the interatomic distances of M–Co introduced in Table 1 are observed as Co–Cu > Co–Fe > Zn–Co > Co–Ni.

The working mechanism of DSSCs in this study, as illustrated in Fig. 7, involves several key components and processes.

The TiO_2 nanoparticle-decorated ITO-coated photoanode serves as the light-harvesting layer. When light is absorbed by the sensitizer dye (here N719), it excites electrons from the dye into the conduction band of the TiO_2. These photo-generated electrons then move through the TiO_2 nanoparticles and are collected at the ITO substrate, flowing into the external circuit to generate electric current. The oxidized dye molecules are regenerated by electrons from the iodide (I^-) in the electrolyte, which is subsequently oxidized to tri-iodide (I_3^-). The tri-iodide ions diffuse towards the spinel cobalt-based metal oxide MCo_2O_4 thin film counter electrodes, where they are reduced back to iodide ions, completing the circuit. This process is facilitated by the high electrocatalytic activity of the MCo_2O_4 counter electrodes, which efficiently catalyzes the reduction of tri-iodide. The high surface area and conductivity of the MCo_2O_4 thin films can play an important role in efficient electron transfer and low charge transfer resistance, contributing to the high performance of the DSSCs. Additionally, the chemical and thermal stability of MCo_2O_4 provides durability and long-term performance stability, making it an excellent choice for counter electrodes in high-performance DSSCs.
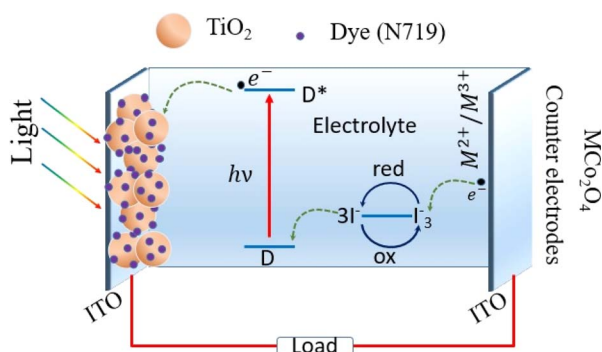
Fig. 7 Schematic diagram of MCo_2O_4 counter-electrode-based DSSC.
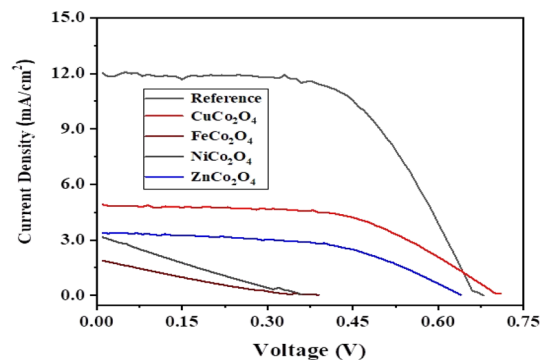
Fig. 8 Current density–voltage plots of DSSCs formed using Pt and $MnCo_2O_4$-based counter electrodes.

Table 2 Some photovoltaic parameters of the DSSCs fabricated using Pt and MCo_2O_4-based counter electrodes

DSSCs	J_{max} mA cm^{-2}	V_{max} mV	J_{sc} mA cm^{-2}	V_{oc} mV	FF	PCE %
$CuCo_2O_4$	4.23	550	4.80	705.8	56.1	1.90
$FeCo_2O_4$	0.99	150	1.96	401.8	18.8	0.15
$NiCo_2O_4$	1.67	160	3.25	364.9	22.6	0.27
$ZnCo_2O_4$	2.83	400	3.41	642.0	51.7	1.13
Pt	10.81	440	12.1	664.1	59.2	4.76

Fig. 8 shows current density–voltage (J–V) plots of the DSSCs fabricated using sensitized MCo_2O_4 based counter electrodes in comparison with Pt-based one as reference solar cell under illumination of 100 mW cm^{-2}. Table 2 summarizes the obtained results and highlights significant differences among the examined thin films. As presented in Table 2, the DSSC with a counter electrode based on $CuCo_2O_4$ nano-leave gives the best photovoltaic response with a J_{max} of 4.23 mA cm^{-2} and a V_{max} of 550 mV which results in 1.9% power conversion efficiency. It is also seen that the open circuit voltage (V_{OC}) value of this device (705.8 mV) superior to the one for conventional DSSC with Pt electrode (664.1 mV). The second-best solar cell efficiency is reported as 1.13% for the DSSC obtained using $ZnCo_2O_4$ hexagonal-like structures. The V_{OC} value of this device with 642.0 mV is very close to the cell with Pt electrode. The other two solar cells obtained from $NiCo_2O_4$ nanosheets and $FeCo_2O_4$ diamond-like structures have lower PCE values of 0.27 and 0.15%, respectively. The lower short-circuit current density (J_{SC}) values observed in our study for DSSCs utilizing alternative counter electrodes, such as $CuCo_2O_4$, $FeCo_2O_4$, $NiCo_2O_4$, and $ZnCo_2O_4$, compared to conventional Pt-based DSSCs. It suggests potential limitations in transport mechanisms associated with these materials. Factors such as differences in catalytic activity, electronic structure, and surface morphology may contribute to the reduced efficiency of photogenerated charge carriers and subsequent lower J_{SC} values. Similar studies have been performed for various metal oxides including binary metal oxides.[58–60] For instance, Kaya *et al.* hydrothermally sensitized $CuCrO_2$ delofossite oxide nanoparticles to use them as photocathode in the fabrication of high efficient tandem p–n photoelectrochemical cells using $CuCrO_2$ delafossite semiconductors as photocathodes coupling with traditional n-type TiO_2 based photoanodes.[59] They reported the efficiency of solar cells between 1.67 and 2.33% for various annealing temperatures.

Considering the structural properties examined in this study across various spinel metal oxides, the samples consistently demonstrated high crystallinity, primarily in the cubic phase. Notably, the identification of active structural planes in these samples indicates a correlation between electrochemical activity and charge injection with these specific planes. For instance, the (311) plane was prominent in the $ZnCo_2O_4$ structure, the (220) plane in $CuCo_2O_4$, both (311) and (220) planes in $NiCo_2O_4$, and the (220) plane in $FeCo_2O_4$. Furthermore, distinctive characteristics and morphologies were observed in the hexagonal structure of $ZnCo_2O_4$ and the nanosheet morphology of $CuCo_2O_4$, which are thought to enhance the photocurrent and efficiency of DSSCs.

Conclusions

The spinel cobalt-based metal oxides of MCo_2O_4 (M: Ni, Cu, Fe, or Zn), were synthesized through the hydrothermal growth technique on ITO substrate to use them as counter electrodes in the fabrication of Pt free DSSCs. The oxides displayed a uniform and homogeneous surface morphology. Interestingly, $NiCo_2O_4$ exhibits nanosheets, Fe Co_2O_4 displays diamond shapes, $CuCo_2O_4$ shows nanoleaves, and $ZnCo_2O_4$ presents a hexagonal shape. These morphologies exhibit unique structural features characterized by a significantly large surface area and the existence of surface defect sites to enhance chemical reactivity. To probe the local structure of the prepared samples, EXAFS data was carried out at Fe and Co K-edge. The absorption Co K-edge was close to the 7721.4 eV value reported in the literature. The Fe Kedge was 7125.53 eV for $FeCo_2O_4$. The pre-edge peak in XANES of the prepared samples suggested T_d Co^{2+}. The shape of the XANES spectrum reveals the spinel structure of the obtained samples. The FT reveals a Co–O_1 coincides with O_h Co^{3+} and Co–O_2 is characteristic for T_d Co^{2+}. On the contrary, Fe–O_1 reveals T_d Fe^{2+} and Fe–O_2 associated with O_h Fe^{3+}. The interatomic distances evaluated from FT analysis of M–Co were observed as Co–Cu > Co–Fe > Zn–Co > Co–Ni. In addition, it is reported that these spinels cobalt-based binary metal oxides, especially $CuCo_2O_4$ nanoleaves and $ZnCo_2O_4$ hexagonal-like structures are promising candidates for the low cost and high efficient DSSCs with 1.9 and 1.13% power conversion efficiency values, respectively.

Data availability

The data that support the findings of this study are available from the corresponding author, Bashar Aljawrneh, upon reasonable request. Researchers interested in accessing the data should contact Bashar Aljawrneh at b.aljawarneh@zuj.edu.jo.

Author contributions

Abdelelah Alshanableh: conceptualization, investigation, methodology, data curation, writing – original draft, writing – review & editing. Yusuf Selim Ocak: conceptualization, investigation, methodology, data curation, writing – original draft, writing – review & editing. Bashar Aljawrneh: conceptualization, investigation, methodology, data curation, writing – original draft, writing – review & editing. Borhan Aldeen Albiss: supervision, investigation, review & editing, funding acquisition.

Khaled Shawakfeh: supervision, investigation, review & editing, funding acquisition. Latif U. Khane: investigation, methodology, data curation, writing – original draft. Messaoud Harfouchee: investigation, methodology, data curation, writing – original draft. Saja Alrousan: investigation, methodology, data curation.

Conflicts of interest

There are no conflicts to declare.

Acknowledgements

References

1 M. Gurulakshmi, A. Meenakshamma, K. Susmitha, N. Charanadhar, V. Srikanth, S. N. Babu, Y. V. Subbaiah, K. Venkateswarlu and M. Raghavender, *Sol. Energy*, 2019, **193**, 568–575.

2 Y. L. Lee, C. L. Chen, L. W. Chong, C. H. Chen, Y. F. Liu and C. F. Chi, *Electrochem. Commun.*, 2010, **12**, 1662–1665.

3 G. Boschloo and A. Hagfeldt, *Acc. Chem. Res.*, 2009, **42**, 1819–1826.

4 R. Güzel, Y. S. Ocak, Ş. N. Karuk, A. Ersöz and R. Say, *J. Power Sources*, 2019, **440**, 227119.

5 R. Güzel, F. Yediyıldız, Y. S. Ocak, F. Yılmaz, A. Ersöz and R. Say, *J. Photochem. Photobiol., A*, 2020, **401**, 112743.

6 M. Grätzel, *J. Photochem. Photobiol., C*, 2003, **4**, 145–153.

7 A. Pérez-Tomás, A. Mingorance, D. Tanenbaum and M. Lira-Cantú, in *The Future of Semiconductor Oxides in Next-Generation Solar Cells*, Elsevier, 2018, pp. 267–356.

8 A. Kunzmann, M. Stanzel, W. Peukert, R. D. Costa and D. M. Guldi, *Adv. Energy Mater.*, 2016, **6**, 1501075.

9 J. Wu, Z. Lan, J. Lin, M. Huang, Y. Huang, L. Fan, G. Luo, Y. Lin, Y. Xie and Y. Wei, *Chem. Soc. Rev.*, 2017, **46**, 5975–6023.

10 S. Rashidi, S. Rashidi, R. K. Heydari, S. Esmaeili, N. Tran, D. Thangi and W. Wei, *Prog. Photovolt.: Res. Appl.*, 2021, **29**, 238–261.

11 M. Wu, M. Sun, H. Zhou, J. Y. Ma and T. Ma, *Adv. Funct. Mater.*, 2020, **30**, 1906451.

12 I. H. Inoue, S. Yasuda, H. Akinaga and H. Takagi, *Phys. Rev. B*, 2008, **77**, 035105.

13 K. Galatsis, Y. Li, W. Wlodarski, E. Comini, G. Sberveglieri, C. Cantalini, S. Santucci and M. Passacantando, *Sens. Actuators, B*, 2002, **83**, 276–280.

14 A. M. A. Ali, N. M. Ahmed, N. A. Kabir, A. M. Al-Diabat, N. A. Algadri, A. Alsadig, O. A. Aldaghri and K. H. Ibnaouf, *Materials*, 2023, **16**, 1868.

15 N. A. Algadri, A. M. AL-Diabat and N. M. Ahmed, *Instrum. Sci. Technol.*, 2023, **51**, 144–161.

16 H. Tüysüz, Y. J. Hwang, S. B. Khan, A. M. Asiri and P. J. N. R. Yang, *J. Nano Res.*, 2013, **6**, 47–54.

17 M. Risch, F. Ringleb, M. Kohlhoff, P. Bogdanoff, P. Chernev, I. Zaharieva and H. Dau, *J. Energy Environ. Sci.*, 2015, **8**, 661–674.

18 W. Liu, J. Han, I. Yamada and S. Yagi, *J. Catal.*, 2021, **394**, 50–57.

19 M. Harada, F. Kotegawa and M. Kuwa, *J. ACS Appl. Energy Mater.*, 2022, **5**, 278–294.

20 W. Deeloed, T. Priamushko, J. Čížek, S. Suramitr and F. Kleitz, *J. ACS Appl. Mater. Interfaces*, 2022, **14**, 23307–23321.

21 Z. Zhang, J. Li, J. Qian, Z. Li, L. Jia, D. Gao and D. Xue, *J. Small*, 2022, **18**, 2104248.

22 L. An, Y. Hu, J. Li, J. Zhu, M. Sun, B. Huang, P. Xi and C. H. Yan, *J. Adv. Mater.*, 2022, **34**, 2202874.

23 S. Lu, Y. Wang, F. Li, G. Yang, H. Yang, X. Zhang and Y. Liu, *J. Phys. Chem. C*, 2017, **121**, 12524–12530.

24 J. Sharma, P. Srivastava, G. Singh, M. S. Akhtar and S. Ameen, *Mater. Sci. Eng., B*, 2015, **193**, 181–188.

25 C. C. Mercado, A. Zakutayev, K. Zhu, C. J. Flynn, J. F. Cahoon and A. J. Nozik, *J. Phys. Chem. C*, 2014, **118**, 25340–25349.

26 F. Yang, X. Tian, Y. Gu, K. Zhang and L. Liu, *RSC Adv.*, 2019, **9**, 24880–24887.

27 L. U. Khan, Z. U. Khan and M. A. Umar, *The Nucleus*, 2023, **60**, 78–85.

28 L. Zhang, Q. Tang, X. Chen, B. Fan, K. Xiao, S. Zhang, W. Deng and A. Hu, *J. Alloys Compd.*, 2017, **722**, 387–393.

29 L. Xie, Y. Liu, H. Bai, C. Li, B. Mao, L. Sun and W. Shi, *J. Colloid Interface Sci.*, 2018, **531**, 64–73.

30 N. R. Chodankar, D. P. Dubal, Y. Kwon and D.-H. Kim, *NPG Asia Mater.*, 2017, **9**, 419.

31 X. Zhang, F. Yang, H. Chen, K. Wang, J. Chen, Y. Wang and S. Song, *Small*, 2020, **16**, 2004188.

32 G. Gao, H. B. Wu and X. W. Lou, *Adv. Energy Mater.*, 2014, **4**, 1400422.

33 D. P. Dubal and R. Holze, *RSC Adv.*, 2012, **2**, 12096–12100.

34 L. Hu, L. Wu, M. Liao, X. Hu and X. Fang, *Adv. Funct. Mater.*, 2012, **22**, 998–1004.

35 B. Palanivel, M. S. Hossain, R. R. Macadangdang Jr., C. Ayappan, V. Krishnan, R. Marnadu, T. Kalaivani, F. A. Alharthi and G. Sreedevi, *ACS Omega*, 2021, **6**, 34563–34571.

36 H. Guo, J. Chen, W. Weng, Q. Wang and S. Li, *Chem. Eng. J.*, 2014, **239**, 192–199.

37 A. N. Naveen and S. Selladurai, *Phys. B*, 2015, **457**, 251–262.

38 A. J. C. Mary and A. C. Bose, *Appl. Surf. Sci.*, 2017, **425**, 201–211.

39 V. Crocella, F. Cavani, G. Cerrato, S. Cocchi, M. Comito, G. Magnacca and C. Morterra, *J. Phys. Chem. C*, 2012, **116**, 14998–15009.

40 S. Verma, H. M. Joshi, T. Jagadale, A. Chawla, R. Chandra and S. Ogale, *J. Phys. Chem. C*, 2008, **112**, 15106–15112.

41 O. C. Pore, A. V. Fulari, C. D. Chavare, D. S. Sawant, S. S. Patil, R. V. Shejwal, V. J. Fularimm and G. H. Lohar, *Chem. Phys. Lett.*, 2023, **824**, 140551.

42 M. S. Burke, M. G. Kast, L. Trotochaud, A. M. Smith and S. W. Boettcher, *J. Am. Chem. Soc.*, 2015, **137**, 3638–3648.

43 M. Risch, K. Klingan, F. Ringleb, P. Chernev, I. Zaharieva, A. Fischer and H. Dau, *J. ChemSusChem*, 2012, **5**, 542–549.

44 G. P. Huffman, N. Shah, J. Zhao, F. E. Huggins, T. E. Hoost, S. Halvorsen and J. G. Goodwin, *J. Catal.*, 1995, **151**, 17–25.

45 X. Wang, Y. Liu, T. Zhang, Y. Luo, Z. Lan, K. Zhang, J. Zuo, L. Jiang and R. J. A. C. Wang, *J. ACS Catal.*, 2017, **7**, 1626–1636.

46 S. Zhang, L. Zhang, H. Li, J. Li, Z. Jiang, W. Chu, Y. Huang, J. Wang and Z. Wu, *J. Synchrotron Radiat.*, 2010, **17**, 600–605.

47 Y. Wang, W.-B. Chen, F.-Y. Liu, D.-W. Yang, Y. Tian, C.-G. Ma, M. Dramićanin and M. G. Brik, *J. Results Phys.*, 2019, **13**, 102180.

48 Q. Zhang, W. Tian, R. Nepal, A. Huq, S. Nagler, J. DiTusa and R. Jin, *J. Chem. Mater.*, 2023, **35**, 2330–2341.

49 L. U. Khan, Z. U. Khan, L. Blois, L. Tabassam, H. F. Brito and S. J. Figueroa, *J. Inorg. Chem.*, 2023, **62**, 2738–2750.

50 H. Y. Wang, S. F. Hung, Y. Y. Hsu, L. Zhang, J. Miao, T. S. Chan, Q. Xiong and B. Liu, *J. Phys. Chem. Lett.*, 2016, **7**, 4847–4853.

51 Y. Liang, H. Wang, J. Zhou, Y. Li, J. Wang, T. Regier and H. Dai, *J. Am. Chem. Soc.*, 2012, **134**, 3517–3523.

52 Y. Lou, J. Ma, X. Cao, L. Wang, Q. Dai, Z. Zhao, Y. Cai, W. Zhan, Y. Guo and P. J. A. C. Hu, *J. ACS Catal.*, 2014, **4**, 4143–4152.

53 A. Y. Khodakov, J. Lynch, D. Bazin, B. Rebours, N. Zanier, B. Moisson and P. Chaumette, *J. Catal.*, 1997, **168**, 16–25.

54 J. Wang, P. A. Chernavskii, A. Y. Khodakov and Y. Wang, *J. Catal.*, 2012, **286**, 51–61.

55 O. Knop, K. I. Reid and Y. N. Sutarno, *J. Can. J. Chem.*, 1968, **46**, 3463–3476.

56 A. V. Chadwick, S. L. Savin, S. Fiddy, R. Alcantara, D. Fernández Lisbona, P. Lavela, G. F. Ortiz and J. L. Tirado, *J. Phys. Chem. C*, 2007, **111**, 4636–4642.

57 J. Zheng, X. Peng, Z. Xu, J. Gong and Z. Wang, *J. ACS Catal.*, 2022, **12**, 10245–10254.

58 A. A. Qureshi, S. Javed, H. M. A. Javed, A. Akram, M. Jamshaid and A. Shaheen, *Opt. Mater.*, 2020, **109**, 110267.

59 I. C. Kaya, S. Akin, H. Akyildiz and S. Sonmezoglu, *Sol. Energy*, 2018, **169**, 196–205.

60 A. Agrawal, S. A. Siddiqui, A. Soni and G. D. Sharma, *Sol. Energy*, 2022, **233**, 378–407.